J Sol-Gel Sci Technol (2009) 50:216–228
DOI 10.1007/s10971-009-1954-x

SPECIAL EDITION: CELEBRATING THE 60TH ANNIVERSARY OF PROFESSOR DAVID AVNIR

Ag nanoparticles deposited onto silica, titania, and zirconia mesoporous films synthesized by sol–gel template method

G. V. Krylova · Yu. I. Gnatyuk · N. P. Smirnova ·
A. M. Eremenko · V. M. Gun'ko

Received: 19 May 2008 / Accepted: 13 March 2009 / Published online: 31 March 2009

Abstract A variety of Ag nanoparticles/oxide mesoporous films with templated silica, titania, and zirconia was synthesized by sol–gel method at glass, aluminum, and silicon substrates using metal alkoxides (tetraethoxysilane, titanium tetraisopropoxide, and zirconium tetrapropoxide) and $AgNO_3$ as precursors of oxide films and Ag nanoparticles, respectively, and Pluronic P123 as a template agent. Oxide films alone and Ag/oxide composites were characterized using hexane adsorption, X-ray diffraction (XRD), Raman and ultraviolet (UV)/vis spectroscopies, scanning electron microscopy (SEM) and transmission electron microscopy (TEM) methods. The distribution of Ag nanoparticles within the films, their sizes, intensity, and position of surface plasmon resonance (SPR) absorbance band at $\lambda = 400$ nm, as well as the textural and structural characteristics of whole films depend on treatment temperature, types of substrates and oxide matrices, oxide crystallization, and Ag content. Ag nanoparticles form preferably on the outer surface of the films under lower sintering temperatures if the amount of loaded silver is low. Oxide crystallization (e.g., TiO_2) promotes silver embedding into the outer film layer. At higher silver content ($\geq$10 at.%) and higher calcination temperature (873 K), silver nanoparticles could be entrapped more uniformly along the film profile because of more intensive evaporation of silver droplets from the outer surface of the films on heating.

Keywords Silica thin film · Titania film · Zirconia film · Ag nanoparticles · Structural characteristics · Optical properties

1 Introduction

Developments of new nanomaterials with metal nanoparticles (Ag, Au, Cu, Rh, Pd, etc.) deposited on oxide surfaces, embedded within pores or encapsulated in polymer and other matrices have gained much attention in material science because of expanding applications of such composites in optics, medical diagnostics, analytical chemistry, catalysis, etc. [1–17]. Incorporation of metal nanoparticles into a solid matrix (e.g., porous silica, titania, zirconia) enhances their stability against the influence of aggressive surroundings, especially oxidation processes. The simultaneous use of several metals entrapped in oxide matrices can give additional effects. For instance, according to Abu-Reziq et al. [17], a synergistic effect is assumed to exist between silica-entrapped metals Pd and Rh, as either of the metallic components is a less active catalyst of the hydrogenation of toluene and other simple benzene derivatives than is the combination of both. Aggregation and reshaping of metal nanoparticles and other processes occurring at the nanometal/porous matrix interfaces on preparation or post-reaction treatments, as well as mutual influence of their electronic structures, physical or

G. V. Krylova · Yu. I. Gnatyuk · N. P. Smirnova ·
A. M. Eremenko · V. M. Gun'ko (✉)
Institute of Surface Chemistry, 17 General Naumov Street,
03164 Kiev, Ukraine
e-mail: gun@voliacable.com; vlad_gunko@ukr.net

G. V. Krylova
e-mail: g_krylova@mail.ru

Yu. I. Gnatyuk
e-mail: yuriy_gnatyuk@yahoo.com

N. P. Smirnova
e-mail: smirnat@i.com.ua

A. M. Eremenko
e-mail: annaerem@voliacable.com

chemical interactions of phases, affect many characteristics of nanocomposites [1–19].

Various synthesis routes such as ion implantation, ion exchange [2], sol–gel, and others [3, 10–14, 17, 20, 21] have been proposed to prepare composites with noble-metal nanoparticles embedded into inorganic matrices. The sol–gel techniques are most effective and popular for preparation of metal/oxide or metal/organics nanocomposites [1–21]. Epifani et al. [1] proposed a general strategy of sol–gel synthesis of Ag and Au nanoparticles within thin oxide films with SiO_2, TiO_2, and ZrO_2 using different ligands (acetylacetone, pyridine, acetonitrile, diethylenetriamine, and dimethyl sulfide) for stabilization of metal ions with stable sols for film deposition. The beginning of the formation of metal nanoparticles was registered at temperatures (873–1,073 K) much higher than temperature of $AgNO_3$ decomposition. Ag nanoparticles formed within the titania and zirconia films were smaller than that for silica. Gonella et al. [21] studied the formation of Ag nanoclusters within ZrO_2 and ZrO_2/SiO_2 matrices depending on their composition and treatment conditions. They found that changes in the ZrO_2/SiO_2 ratio effectively control the size of Ag nanoparticles as a result of varied matrix crystallinity. Nevertheless a broad band of the surface plasmon resonance (SPR) of Ag clusters was observed in the spectra of prepared composites. Investigations of TiO_2/Ag nanocomposites synthesized utilizing different techniques [2, 3] showed that broad and red-shifted SPR bands of Ag nanoparticles were observed in the spectra of these films. This optical behavior reveals a broad size distribution and nonuniform allocation of metal nanoparticles within the films (because of aggregation, agglomeration, and other processes).

Recently we have studied thin mesoporous oxide films (templated silica and titania) as promising substrates for photoactive molecules and photocatalysts [22, 23]. Pore structure of similar films could be appropriate for the formation of silver nanoparticles with a uniform size distribution prepared at relatively low temperatures and without treatment in hydrogen atmosphere. The reason is that burning of template and other organic components generates large amounts of volatile species (incompletely oxidized) which can play a role of silver reduction initiators. Elucidation of the factors governing the particle size distribution and metal nanoparticle/oxide matrix interactions is of importance for synthesis of nanocomposites with required morphological, optical, and other characteristics [15, 16]. Therefore the aim of the present paper was to study (1) features of sol–gel technique on template synthesis of SiO_2, TiO_2 and ZrO_2 mesoporous films with incorporated silver nanoparticles over a broad range of concentration (1–30 at.% Ag) but with a narrow size distributions of Ag particles formed over a narrow temperature range (770–870 K) on one-step heat-treatment process in the air atmosphere, and (2) the optical properties of these materials.

2 Experimental

2.1 Synthesis of materials

All reagents (Aldrich, reagent grade) were used as received. Template sol–gel method was applied for preparation of mesoporous silica, titania, and zirconia films at glass, silicon, and aluminum substrates. Such alkoxides as tetraethoxysilane (TEOS), titanium tetraisopropoxide (TTIP), and zirconium tetrapropoxide (ZTP) were mixed in a water–ethanol solution for prehydrolysis. HNO_3 solution (1 M) was used to adjust pH value on hydrolysis of TEOS. Hydrolysis of TTIP and ZTP is very fast in the presence of water, resulting in formation of precipitated hydroxides. To prevent this process, acetylacetone (acac) as a complexing agent [24] was added to the solution. Ethanol solution of a template agent (nonionic triblock copolymer of propyleneoxide with ethyleneoxide $EO_{20}PO_{70}EO_{20}$, Pluronic P123) used to form ordered mesopores in the films was added to the solution of alkoxides after their prehydrolysis for 4–16 h. The final molar ratio of components was 1 (TEOS, TTIP, ZTP):0.008 or 0.05 (P123):0.016 or 0 (HNO_3):15 or 10 (H_2O):15 or 41 (C_2H_5OH):0 or 0.5 (acac) on the synthesis of SiO_2 or TiO_2 (ZrO_2) films, respectively.

To form Ag nanoparticles embedded within the oxide films, an appropriate amount of $AgNO_3$ was added to the precursor sols. Concentration of Ag^+ ions was varied from 1 at.% to 30 at.% compared with molar concentration of alkoxides. This way of Ag^+ source introduction into the sol allows us to suppose a constant thickness of the oxide films, and consideration of the absorbance spectra of the Ag/oxide films is based on this assumption.

For film deposition onto glass, silicon wafer or aluminum substrates, a dip-coating technique was utilized. After deposition, gelation, and gel ripening, the films were dried in air at room temperature for 2 h (dried samples). Then the dried films were sintered in a furnace at a heating rate $\beta = 2$ K/min to 523 K, and at $\beta = 0.25$ K/min from 523 to 623 K. P123 burns out at these temperatures and this process should be carried out carefully to keep the ordered porous structure of the oxide film/Ag nanoparticles. Then temperature was elevated to 773, 823, and 873 K at $\beta = 3$ K/min and the systems were kept at a certain temperature for 3 h.

2.2 Characterization techniques

Mesoporous structure of the SiO_2, TiO_2 and ZrO_2 films was determined from the small-angle ($0.4 < 2\theta < 10°$) XRD patterns recorded using a DRON-3 M (Burevestnik, St. Petersburg) diffractometer with Cu K_α ($\lambda = 0.15418$ nm) radiation. XRD analysis of crystalline phases was performed using a DRON-4-07 (Burevestnik, St. Petersburg) diffractometer (Cu K_α radiation with a Ni filter) with Brag-Brentano registration geometry ($2\theta = 10$–$60°$). The average size of crystallites was determined using Sherrer equation applied to the most intensive peak.

The crystalline structure of silver nanoparticles/oxide films deposited onto glass slides was studied using a Renishaw InVia Raman microscope (Wotton-under-Edge, UK). A 488-nm Ar^+ laser (900 μW) was used for sample excitation, and the power was measured using a Newport optical power meter at the sample plane (scan range 100–1,000 cm^{-1}, measurements repeated five times).

To estimate the specific surface area (S_{BET}), the pore volume (V_p), and the pore size distribution (PSD) of silica and titania films, adsorption–desorption isotherms of hexane vapor were recorded at 293 K using an apparatus equipped with a McBain-Bakr quartz microbalance (sensitivity 2.3 mg/mm) and a cathetometer. The samples were degassed before the adsorption at 0.001 Torr and 473 K for 2 h. The specific surface area [25] was calculated from the hexane adsorption at relative pressures $p/p_0 = 0.04$–0.2. The PSD was calculated from the hexane desorption data using a method proposed by Nguyen and Do for carbon materials with slit-shaped pores [26] and modified [27] to use the model of cylindrical pores with the Lennard–Jones parameters of hexane/silica or titania.

For microscopic investigations, the films were deposited onto the silicon wafers. SEM images were recorded using a JEOL 1530 scanning electron microscope (accelerating voltage 100 kV). TEM images recorded using a JEM-100CXII electron microscope were obtained for the films scratched out from the glass substrates and deposited from ethanol suspension onto a carbon-covered copper grid.

Optical spectra (transmission mode) of the films were recorded using a Lambda UV/vis (Perkin–Elmer) spectrometer.

3 Results and discussion

3.1 Structural characteristics of SiO_2 and TiO_2 films

In contrast to individual amorphous silica, crystallization of titania or zirconia can negatively affect ordered mesostructure (templated by Pluronic P123) because crystal growth with elevating temperature leads to injury of the pore walls. Formed mesostructure can be analyzed using XRD patterns (Fig. 1). Two sharp maxima can be distinguished at low 2θ values (Fig. 1a) corresponding to d_{100} and d_{110} spacing of 15.0 and 9.2 nm for a weakly ordered hexagonal mesostructure at the pore-centre-to-pore-centre distance $a = 17.5$ nm. A nonsintered TiO_2 film exhibits three peaks at $2\theta < 2°$, corresponding to a lamellar mesostructure [28] at $a = 23.1$ nm. Additionally, there are several lines at higher 2θ values (Fig. 1b) which correspond to smaller d values.

After calcination of the titania and silica films at 673 K only one peak (at a higher 2θ value in comparison with dried samples) is observed in the XRD patterns (Fig. 1a, b inserts). This peak corresponds to $d_{100} = 13.8$ nm (SiO_2) and 14.9 nm (TiO_2). One could assume that a certain pore organization remains, although the ordered mesostructure was completely lost. Yang [29] and Yamada [30] considered similar structures as a one-dimensional hexagonal mesostructure characteristic for films which, in contrast to

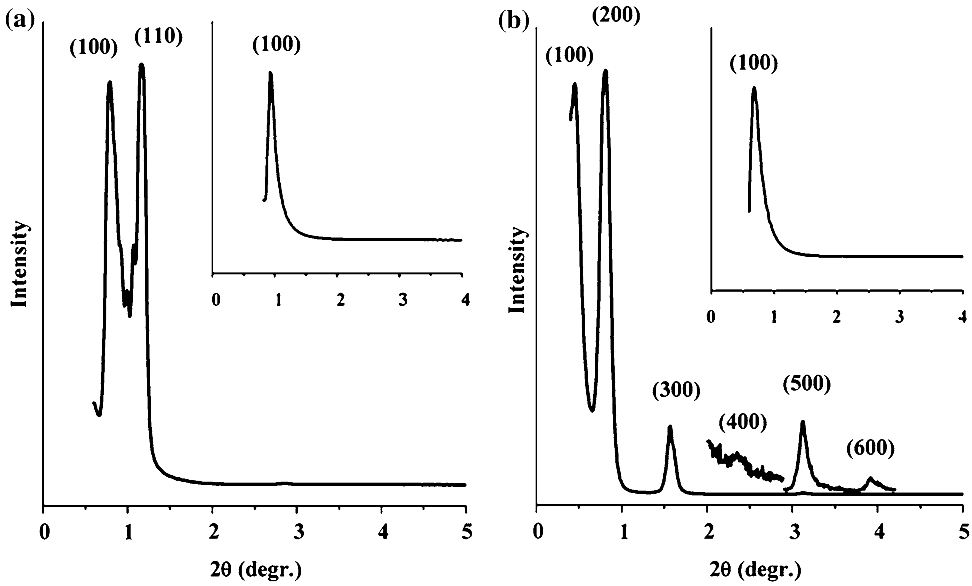

Fig. 1 Low-angle XRD patterns of **a** silica and **b** titania films dried and heated at 673 K (*insert*)

powders, lack (110), (210), and (220) reflections in the spectra because of the parallel orientation of pore channels to the substrate surface. A certain displacement of the first diffraction maximum after sample calcination at 673 K suggests that the films become not only less ordered but also denser after removal of residual solvent and template burning-out [28, 31, 32].

The structural characteristics of mesoporous silica and titania films were studied using hexane vapor adsorption–desorption isotherms (Fig. 2a), which could be assigned to the type IV of the IUPAC classification. The shapes of the isotherms and the PSDs (Fig. 2b) depict a mesoporous character of the template-generated porosity stable on heating at 773 K. The pore structure of the silica and titania films differs because of a larger contribution of broader mesopores in the titania film (titania sample 1, curves 2) possessing a larger pore volume and specific surface area than the silica film has (Table 1). However, titania prepared on the glass substrate (titania sample 2, curves 3) is characterized by a smaller porosity than silica or titania formed on the aluminum substrate. Thus, the structural differences in the silica and titania films can be due to the differences not only in composition of reaction media (especially Pluronic P123 content) but also in the substrate effects. The PSDs of both materials are multimodal because of the formation of main channels related to weakly ordered mesostructure, narrower pores in their walls, and certain destruction of the pore walls (e.g., on titania crystallization and template burning out) on calcination at 673 K (reflected in the XRD patterns). Titania crystallization leads to a higher fractal dimension ($D = 2.58$ and 2.48 for samples 1 and 2, respectively) than that of silica ($D = 2.42$) calculated using the hexane adsorption data with the Frenkel–Halsey–Hill equation described in detail by Avnir and Jaroniec [33]. Additionally, deviation of the pore shape from the model of cylindrical pores [27]

$$\Delta w = \frac{S_{\mathrm{BET}}}{S^*} - 1 = \frac{S_{\mathrm{BET}}}{\int_{R_{\min}}^{R_{\max}} f_{\mathrm{S}}(R)\mathrm{d}R} - 1 = \frac{S_{\mathrm{BET}}}{\int_{R_{\min}}^{R_{\max}} \frac{w}{R}\left(f_{\mathrm{V}}(R) - \frac{V(R)}{R}\right)\mathrm{d}R} - 1 \qquad (1)$$

[where $R_{\max}$ and $R_{\min}$ are the maximal and minimal pore radii, respectively; $V(R)$ is the volume of pores at the radius R; $w = 2$ for cylindrical pores; and $f_{\mathrm{S}}(R)$ and $f_{\mathrm{V}}(R)$ are the PSDs with respect to the surface area and pore volume] shows that the titania film is more disordered and the pore

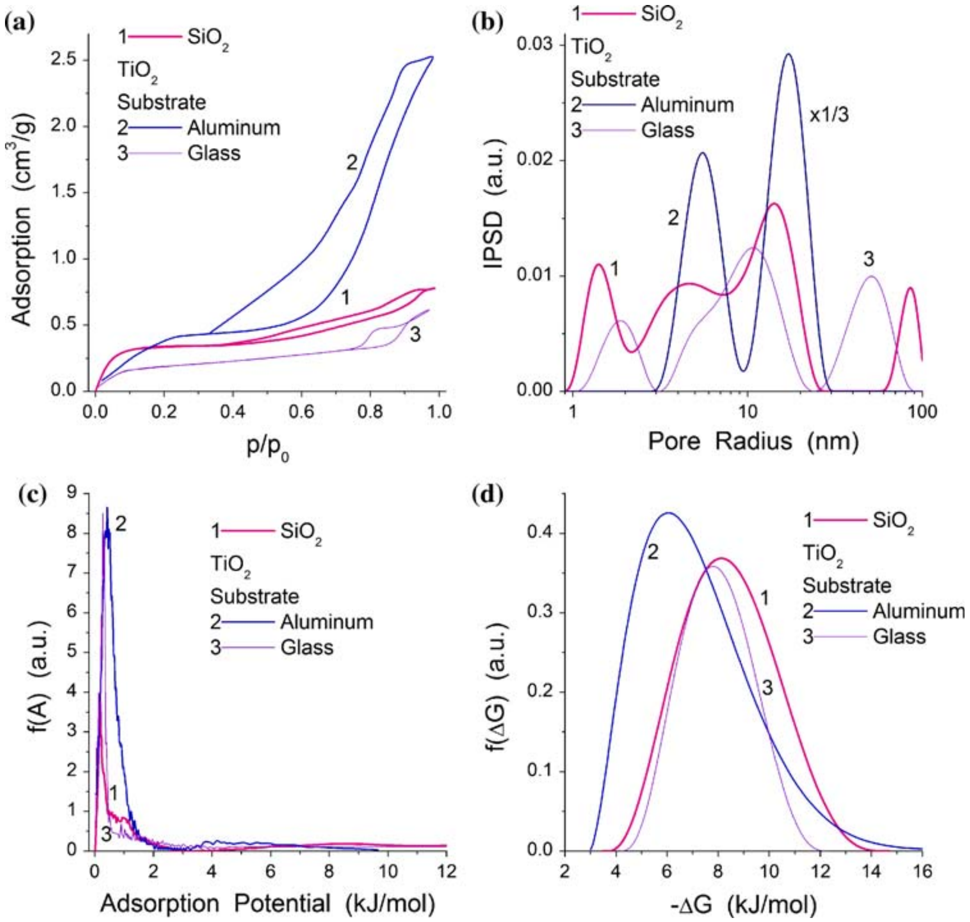

Fig. 2 **a** Hexane adsorption isotherms, and the distribution functions of **b** pore size of SiO_2 (*1* glass substrate) and TiO_2 [curves *2* (aluminum substrate) and *3* (glass substrate)] films sintered at 773 K, **c** adsorption potential, and **d** Gibbs free energy of hexane adsorption

Table 1 Structural characteristics of silica and titania films

Film	S_{BET} (m^2/g)	V_{mic} (cm^3/g)	V_{mes} (cm^3/g)	V_{mac} (cm^3/g)	t_w (nm)	a (nm)
SiO_2	650	0.003	0.797	0.075	4.8	16.2
TiO_2 (sample 1)	800	0	2.546	0.014	5.0	17.5
TiO_2 (sample 2)	393	0	0.471	0.184		

Note: V_{mic}, V_{mes}, and V_{mac} are the volumes of micropores at the pore radius $R < 1$ nm, mesopores at $1 < R < 25$ nm, and macropores at $R > 25$ nm, respectively, t_w is the pore wall thickness, and $a = d_{100}\frac{2}{\sqrt{3}}$ is the cell parameter

walls are rougher since $\Delta w = 0.584$ (titania sample 1) and 0.387 (silica). The roughness of the pore walls, estimated as $\chi = 100(S_{BET} - S^*)/S_{BET} = 100\Delta w_{cyl}/(\Delta w_{cyl} + 1)$ (%), corresponds to 36.9 (titania) and 27.9% (silica). These values are much larger than that for, e.g., much more ordered mesoporous silica SBA-15 (synthesized using a similar template technique with Pluronic P123 but without a substrate) in the form of microparticles characterized by a very small value $\Delta w = 0.02$ [34]. In other words, the pore structure in thin templated films deposited onto a substrate can be less ordered than that of the same individual materials synthesized in the form of individual particles because of the strong influence of a substrate on the thin-film structure damaged on drying and calcination stages. These effects depend also on the structural and crystalline differences of deposits and substrates (e.g., observed for two mentioned titania samples).

The observed structural differences of the films reflect in adsorption characteristics such as the distribution functions of the hexane adsorption potential [$f(A)$] (Fig. 2c) and the Gibbs free energy of hexane adsorption [$f(\Delta G)$] (Fig. 2d). A very low contribution of micropores (as well as a relatively large size of hexane molecules, which diminishes the accessibility of narrow pores in comparison with N_2 or Ar used as typical adsorbates for the analysis of the structural characteristics) causes relatively low boundary A and ΔG values. These values are relatively close for both films because of the main contribution of nonspecific dispersive interaction of hexane with the silica and titania surfaces.

The cell parameter a (Table 1) was calculated using the d_{100} values for sintered SiO_2 and TiO_2 films assuming that the mesostructure corresponds to the hexagonal symmetry of pore location. Observed reduction of the cell parameter after calcination reveals general contraction of the mesoporous structure of the films by 8% and 25% for silica and titania films, respectively. The wall thickness was estimated from SEM images of the sintered films (Fig. 3) and compared with values calculated using hexane adsorption measurements and cell parameters from low-angle XRD measurements. The a values (as the pore-centre-to-pore-centre distances) correspond to the first PSD peak for the titania film and the second one for silica. If the mean pore size is ~10 nm (silica) and ~12 nm (titania) from the PSDs (Fig. 2), then the a values give pore wall thickness of 6.2 and 5.5 nm, respectively, which are close to those estimated from SEM images of the sintered films. This result is indirect evidence of keeping low-ordered mesostructure of the films. Thus all the characteristics (Figs. 2 and 3; Table 1) show that silica and titania films are mesoporous with small contributions of micropores and macropores.

SEM images (Fig. 3a) show that the silica film structure is slightly ordered, keeping certain patches of the hexagonal mesostructure significantly disordered on heating. Stronger damages of the mesostructure, transformed from lamellar to worm-like, are observed for titania (Fig. 3b) than for amorphous silica (Fig. 3a) because of crystallization of titania.

3.2 Structural characteristics of Ag nanoparticles/oxide films

The sol–gel synthesis with mixing of components on the molecular level allows the formation of nanocomposites

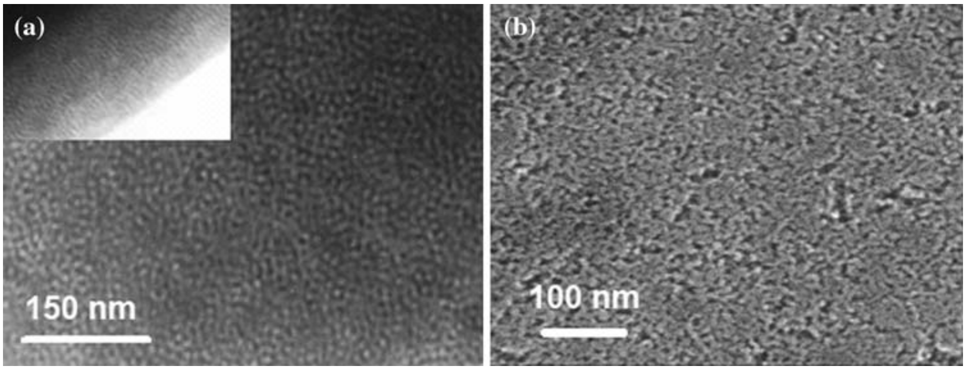

Fig. 3 SEM images of mesoporous films of **a** silica (*insert* shows normal cross-section of the film) and **b** titania

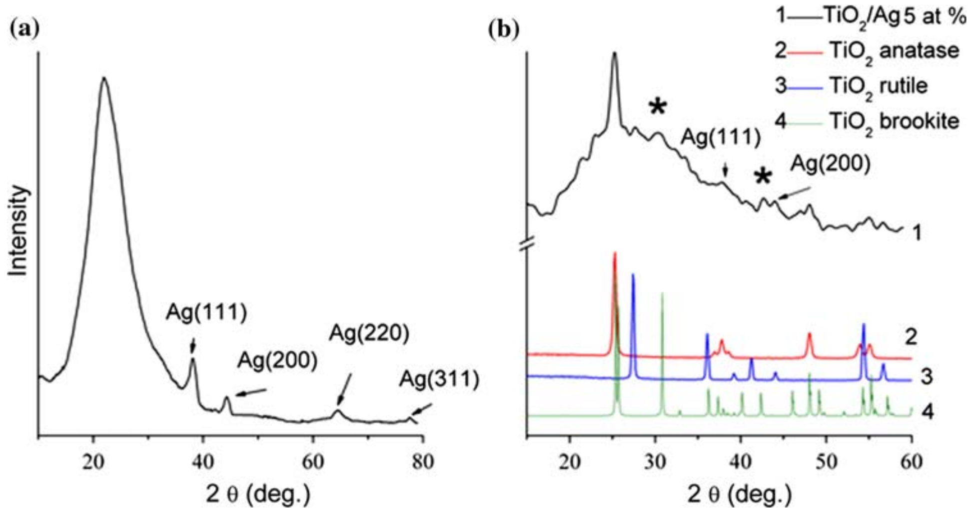

Fig. 4 XRD patterns of **a** SiO_2/Ag 10%, **b** six-layered TiO_2/Ag 5% film (curve°*1*) treated at 773 K; curves°*2*, *3* and *4* correspond to anatase, rutile, and brookite, respectively, and asterisks label brookite lines

with metal/dielectric or metal/semiconductor over a wide range of their content. An initial distribution of cations of noble metals can be uniform in the depth profile. However, reduction of cations causes their consolidation because the free energy of solvation (ΔG_s) of Ag^+ in water is negative and very low ($\Delta G_s = -75.7$ kcal/mol, calculated using the B3LYP/SDD/IEFPCM method [35, 36]), whereas for Ag^0 it is positive ($\Delta G_s = 4.3$ kcal/mol), and $\Delta G_s = 8.1$ kcal/mol (Ag_4^0), -42.3 kcal/mol (Ag_4^+), 22.5 kcal/mol (Ag_8^0), and -24.4 kcal/mol (Ag_8^+). Consequently, the average positive value of the free energy of solvation per Ag atom for reduced metal clusters decreases with growing size of them. Additionally, the solvation effects differ in narrow and broad pores and at the outer surface of the films because of the differences in the structure of the solvation shells of cations, and charged and reduced Ag clusters there. Then, on the heating stage, Ag clusters and particles can change their morphology and location in the film (in pores or at the outer surface of the film depending on the size of particles and pores, mass transfer processes, etc.).

The presence of entrapped metallic silver in the nanocomposites with SiO_2/Ag and TiO_2/Ag after thermal treatment was confirmed by appearance of characteristic reflexes of the cubic Ag phase in the XRD patterns (Fig. 4) at $2\theta = 38.11°$ (111), 44.37° (200), 64.35° (220), and 77.54° (311). For TiO_2/Ag 5 at.% film, the crystallization of titania (mainly anatase appearing at $2\theta = 25.3°$, 48.0°, 53.9°, and 55.0° corresponding to (101), (200), (105), and (211), respectively) occurs simultaneously with silver nanoparticles formation. It should be noted that low-intensive lines at $2\theta = 27.8°$ and 56.7° and at $2\theta = 30.4°$ and 42.8° attributable to rutile and brookite phases of TiO_2 do not allow us to state the presence of these titania in the samples while Raman spectroscopy (vide infra) clearly indicates the presence of anatase and brookite. Promoting of anatase-to-rutile phase transition by low-valence cations (e.g., Ag^+) occurs due to the mechanism of charge compensation when the vacancies form and affect the atom transport [37]. A shape of the XRD spectrum of TiO_2/Ag 5% film at $2\theta = 20–35°$ suggests also the presence of amorphous titania.

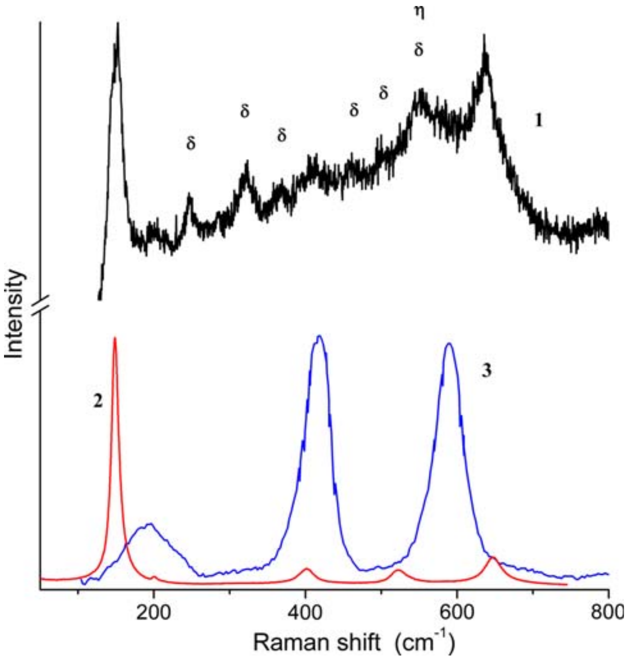

Fig. 5 Raman spectra of TiO_2/Ag (5 at.%) film after thermal treatment at 773 K (curve *1*) (δ, TiO_2 brookite; η, glass substrate); anatase (*2*) and rutile (*3*)

The Raman spectrum of TiO_2/Ag 5% film deposited onto the glass substrate and sintered at 773 K (Fig. 5) depicts a set of reflexes related to anatase and brookite (lines at 150, 198, 409, and 636 cm^{-1}, corresponding to E_g, B_{1g}, A_{1g} or B_{1g}, and E_g modes of anatase [38, 39] and weaker reflexes at 247, 323, 366, 459, 501, and 543 cm^{-1}, corresponding to brookite [40, 41]). Notice that the Raman spectra of Ag/ZrO_2

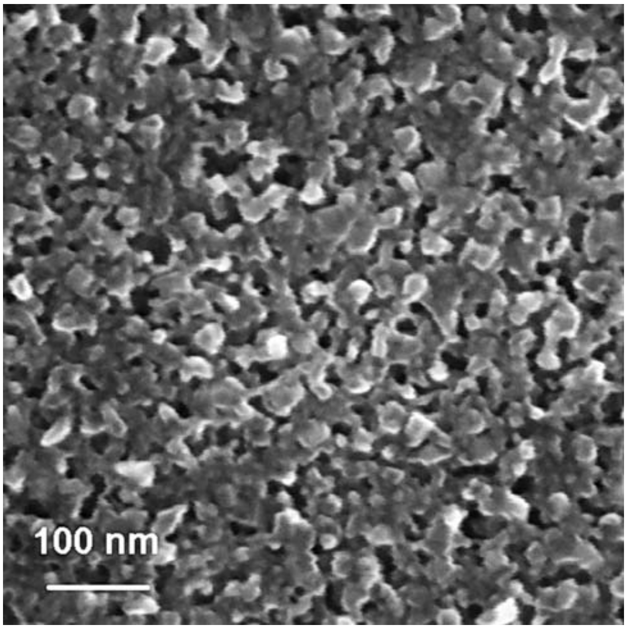

Fig. 6 SEM image of TiO_2/Ag 5% film

films (not shown here) did not give clear information on crystalline structure of zirconia; therefore, these films could be considered as mainly amorphous.

Composites with silver nanoparticles/porous oxide films demonstrate certain changes in the pore structure in comparison with individual oxide films. In the case of silica, silver doping leads to the formation of secondary porosity with much larger pores. The Ag/TiO_2 film (Fig. 6) includes titania crystallites of 15–25 nm in size, which form aggregates (dark gray color on SEM image) with smaller silver particles (white and light gray), and the pore sizes are over the 10–30 nm range. Thus addition of silver salt to the reaction media (i.e., the formation of Ag nanoparticles) leads to enlargement of the pore size but the high-ordered mesostructure does not form (Fig. 6).

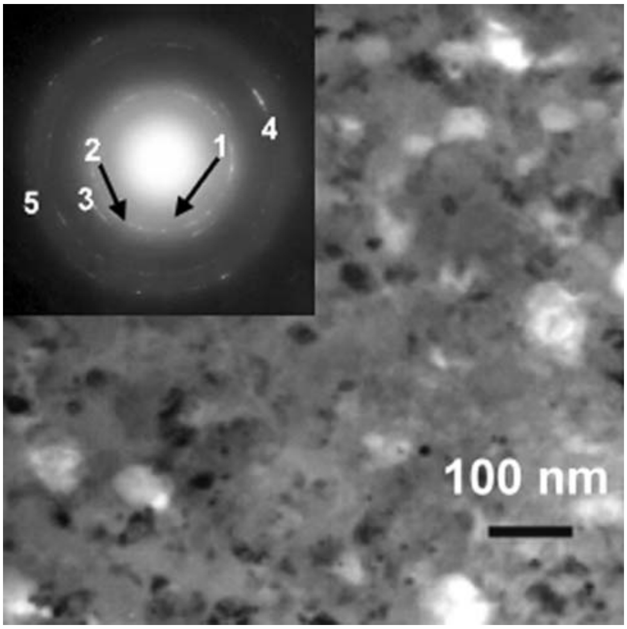

Fig. 8 TEM image and electron diffraction pattern (*insert*) of TiO_2/Ag 5% film sintered at 773 K: *1* Ag (111) and TiO_2 (004); *2* Ag (200); *3* TiO_2 (105); *4* TiO_2 (215); *5* TiO_2 (305)

A relatively uniform distribution of silver nanoparticles deposited predominantly at the outer surface and entrapped in a near-surface layer in the thin silica and titania films is confirmed by SEM images (Fig. 7). The analysis of these images was done considering that heavy elements (in our case Ag) backscatter electrons more strongly than light elements (O, Si, Ti), and thus appear brighter in the image [42]. The average size of Ag nanoparticles at the silica matrix is larger (5–9 nm) than that at titania (3–5 nm).

TEM images (combined with the electron diffraction data) of the films (Fig. 8) confirm the formation of crystalline titania (anatase) and deposition of metallic silver nanoparticles. The size of Ag nanoparticles in the TiO_2/Ag 5% film varies in the 4–10 nm range, which is in

Fig. 7 SEM images of mesoporous films sintered at 773 K: **a** SiO_2/Ag 10% and **b** TiO_2/Ag 10%

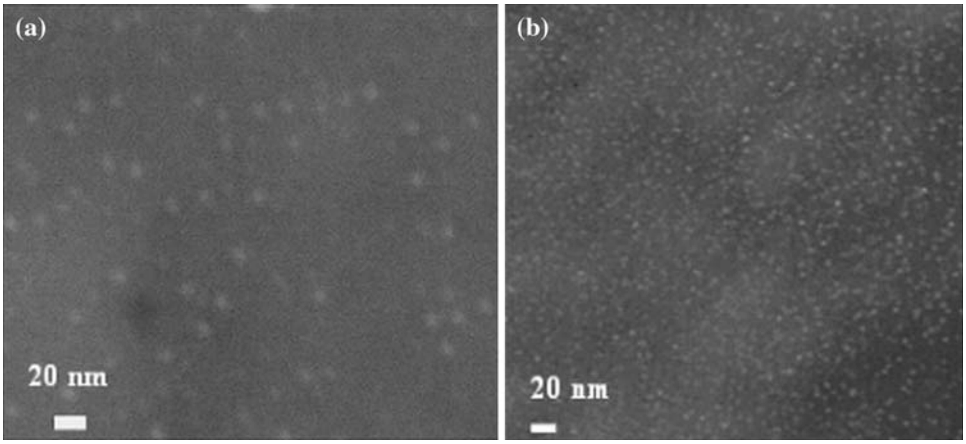

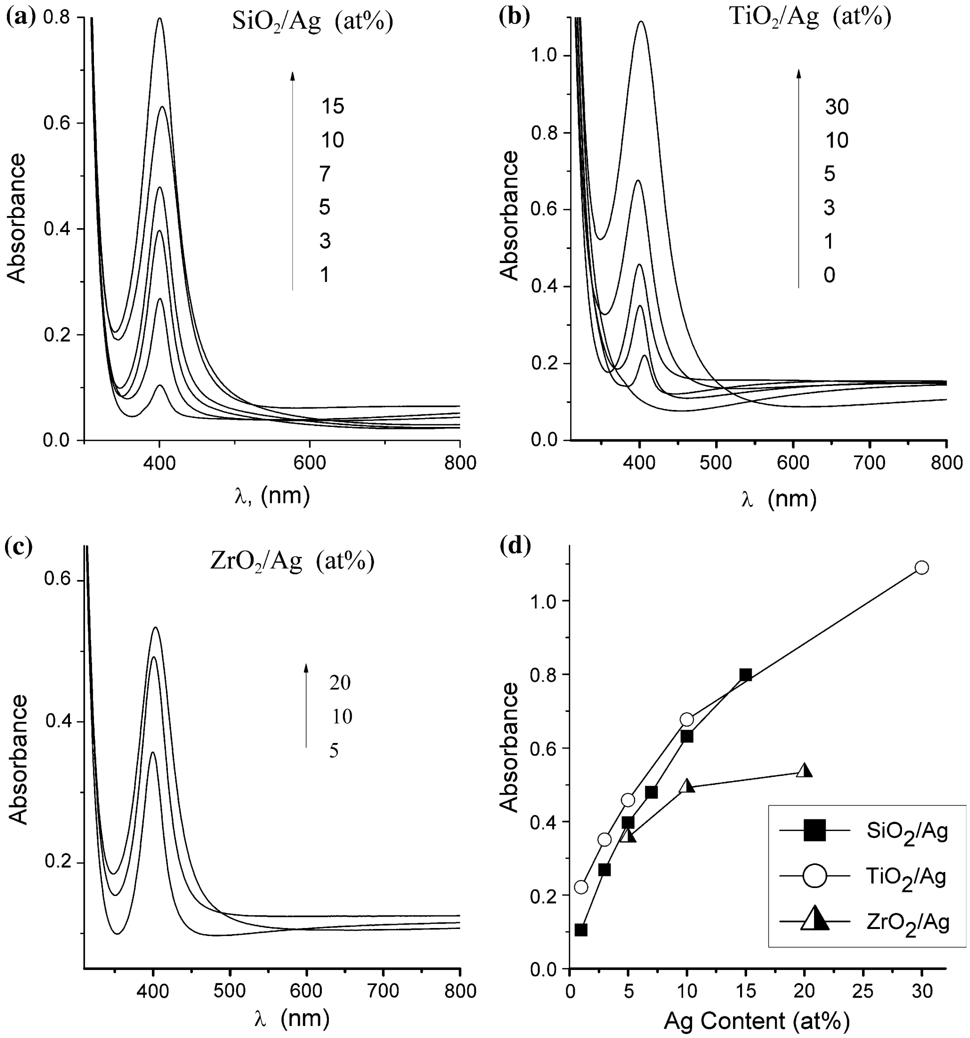

Fig. 9 Absorbance spectra of films with increasing Ag^+ content in the initial sol for **a** SiO_2/Ag; **b** TiO_2/Ag; **c** and ZrO_2/Ag; and **d** maximal SPR band intensity versus silver content in the films sintered at 773 K in air for 2 h

agreement with the results of optical spectroscopy discussed below and with the literature data [2, 15].

The morphology of Ag nanoparticles could be monitored using the SPR absorbance band at 400 nm accompanied by yellow coloration of a film. On low Ag doping, a film is transparent or exhibits only pale yellow tint.

3.3 Optical properties of Ag nanoparticles/porous oxide films

The optical properties of Ag-containing SiO_2, TiO_2, and ZrO_2 films as well as the morphology of Ag nanoparticles depend on the amounts of Ag^+ added to the reaction media (Fig. 9). The maximal intensity of absorbance at 400 nm is observed for the Ag/titania and Ag/zirconia films treated at 773 K and for Ag/silica treated at 823 K. One can assume that certain amounts of silver ions remain unreduced after treatment at 773 K. However the dependence of the SPR band intensity on the amount of Ag (Fig. 9d) shows that the percentage of unreduced ions remains nearly constant for the Ag/silica and Ag/titania films at different silver loading. The Ag/ZrO_2 films exhibit a significant deviation from the dependence observed for the SiO_2 and TiO_2 films, probably due to a higher amount of unreduced Ag^+ than the silica and titania matrices include. In the absence of effective complexing ligands, silver ion can form complexes with oxygen atoms of metal alkoxides and products of their hydrolysis [21] or polar functionalities of template molecules. Silver ions can form inclusions in the pore walls of the oxide matrices at increased amounts as follows: $SiO_2 \rightarrow TiO_2 \rightarrow ZrO_2$.

Silver ion reduction is caused by electron attachment from organic substances or the products of their burning. The reduction could occur at lower temperatures due to electron liberation from titania and zirconia possessing relatively narrow band gaps. Initiation of silver ion reduction demands strong reductive agents because the Ag^+/Ag^0_{atom} potential is −1.8 V [43]. As first clusters are formed the potential grows to 0.79 V (water solution) for Ag^+/Ag^0_{metal}, and the reduction process is facilitated.

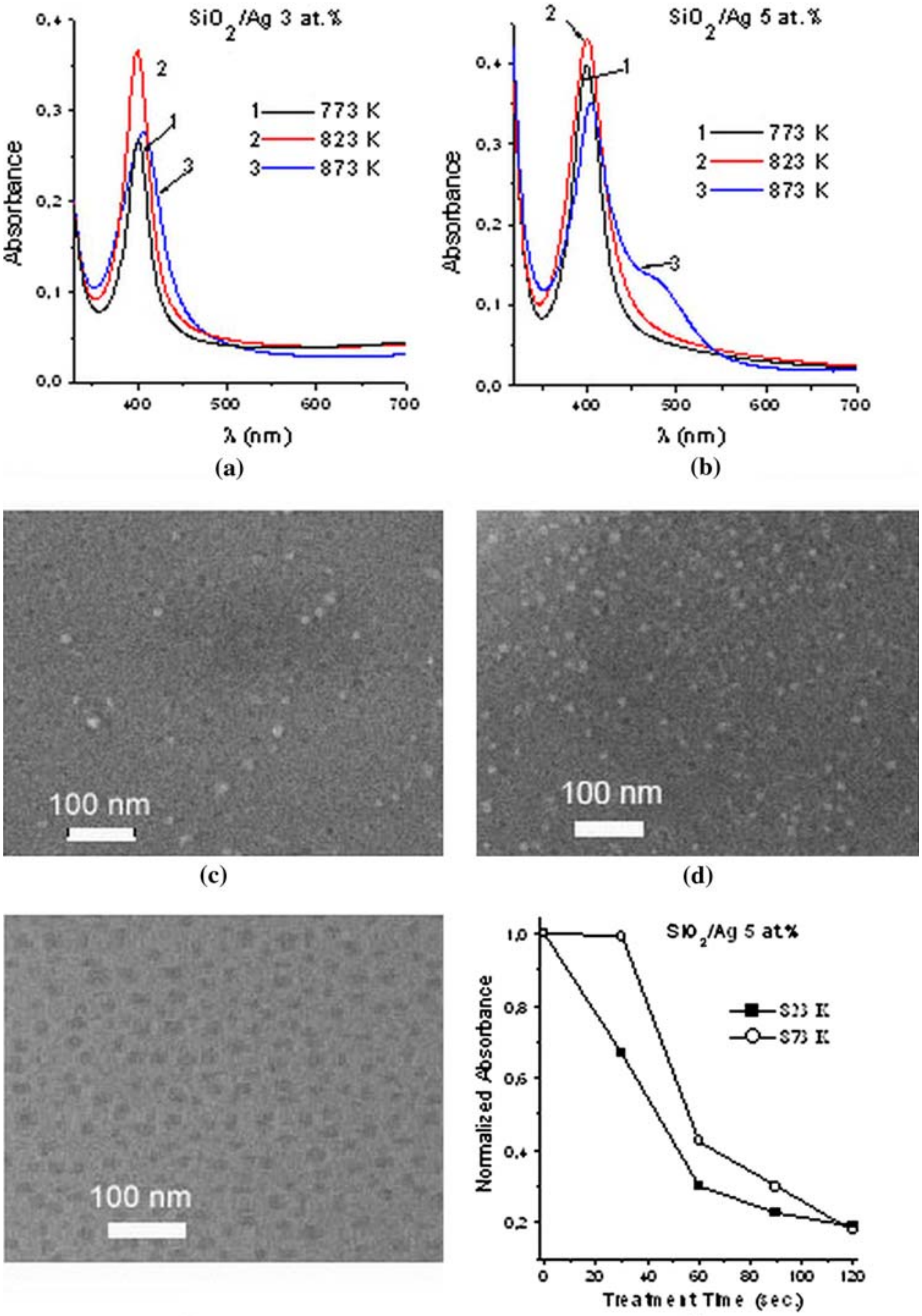

(a) (b) (c) (d) (e) (f)

Fig. 10 **a**, **b** Spectral changes in SiO$_2$/Ag films with treatment temperature; **c** SEM images of SiO$_2$/Ag 3% film treated at 773 K and **d**, **e** SiO$_2$/Ag 5% film treated at **d** 773 K and **e** 873 K; **f** diminution of absorbance with time of film etching in aqueous solution of 10% HF and 2.5% HNO$_3$

Further growth of Ag clusters to nanoparticles can proceed due to silver ion reduction with the participation of the TiO$_2$ or ZrO$_2$ matrices. The bond energy of Ag–O is low and more preferable bonding corresponds to Ag–Ag. Therefore, on thermal treatment, the silver atoms and clusters will tend to agglomerate to form metal nanoparticles [3]. Elevating temperature of sintering of silica, titania, and zirconia with embedded Ag nanoparticles causes certain spectral changes in the SPR band shape, position, and intensity.

For the Ag/silica film, the SPR band is the most intensive after thermal treatment at 823 K (Fig. 10a). Elevating temperature to 873 K leads not only to a decrease in the SPR intensity but also to the peak displacement towards larger wavelength. An increase in the Ag loading leads to appearance of a shoulder at 470–520 nm (Fig. 10b). A decrease in the integral absorbance of the SiO_2/3% Ag film over the 350–600 nm range is observed with elevating temperature, but this value is constant for the SiO_2/5% Ag film. Thus in the case of a film with lower content of Ag, the total amount of reduced silver atoms decreases but it does not practically change for the silica/5% Ag film. Such effect can be clarified using SEM image of the films (Fig. 10). At the surface, there are some amounts of silver nanoparticles of 10–15 nm size (porous mesostructure is partially destroyed due to growth of these nanoparticles) and some amount of voids of a shape corresponding to that of Ag nanoparticles. These voids can remain after removal of Ag nanoparticles on heating. The silica surface is hydrophilic but reduced Ag particles are hydrophobic. Therefore forces within mesopores should push out these particles onto the outer surface of the film, from where they are removed into the gas phase. A clean glass plate placed in close proximity to the glass substrate covered with Ag-containing film when heated becomes pale yellow due to precipitation of silver from vapors with the formation of nanosized islands. This could be the reason for the decrease in the integral absorbance of the SiO_2/3% Ag film heated at a higher temperature. The fact that, in the case of the SiO_2/5% Ag film, elevating temperature (from 823 to 873 K) does not change the integral absorbance could be explained by a higher content of Ag^+ in the initial sol and a higher percentage of them embedded into the silica matrix. These Ag particles could be removed only under higher temperatures. This assumption is confirmed by SEM images of the SiO_2/5% Ag film (Fig. 10d, e) showing that the film treated at 773 K has a low number of surface voids in comparison with the number of Ag nanoparticles. The film sintered at 873 K has only voids at the surface, although the presence of silver nanoparticles within pores was proved by the appearance of the SPR maximum. Additional evidence for this hypothesis was obtained by etching of films in solution of 10% HF:2.5% HNO_3 (Fig. 10f), showing that yellow color of 823 K-sintered film disappears gradually during the first minute of treatment. However, the film sintered at 873 K does not exhibit a decrease in SPR intensity during the first 30 s of etching, but it then starts and continues until 2 min of immersion. This reveals that Ag nanoparticles responsible for yellow color of the first film locate mainly within the surface layer. In the second case, Ag particles locate within a deeper layer in the film. Red shift, broadening or even occurrence of an additional mode in the SPR band indicates that nonspherical particles might be formed in the films because such effects are characteristic for ellipsoid [15] or rod-shaped nanoparticles [44]. The formation of Ag particles of such a shape confined in the film volume can be expected whereas their growth is restricted by the shape and size of pores there.

General tendencies of the thermal changes in the Ag/ZrO_2 films are similar to those of Ag/SiO_2 but the highest intensity of the SPR band was observed after sintering at 773 K (Fig. 11). Additionally, amorphous state of the Ag/ZrO_2 films calcined at 773 K was confirmed by Raman spectroscopy data, as is expected for silica films. The SPR intensity and integral absorbance decrease with elevating temperature to 823 K. However, calcination at 873 K results in an increase in integral intensity.

In the case of the Ag/TiO_2 films, a sharp decrease occurs for both SPR maximum and integral absorbance with elevating sintering temperature (from 773 to 873 K), especially for the TiO_2/3% Ag film. Significantly smaller Ag nanoparticles form in the titania films because of the effects caused by intensive crystallization of titania (Figs. 6, 7b). Previously it was shown [3] that, for TiO_2/8% Ag film of 120 nm thickness, the Ag content in the outer 30-nm-thick layer was increased to 20 at.%. XPS measurements showed [20] that, in TiO_2/0.06 at.% Ag film, the surface layer is enriched with silver at the Ag-to-Ti ratio of 1.13. These data suggest that enhanced evaporation of silver occurs from the outer surface of the titania film; and, the more nonuniform the silver distribution, the lower the silver content [3, 20]. Disappearance of the SPR band for the titania/3% Ag film could be also caused by partial "dissolution" of silver droplets of a certain critical size in the crystalline matrix, as described elsewhere [2].

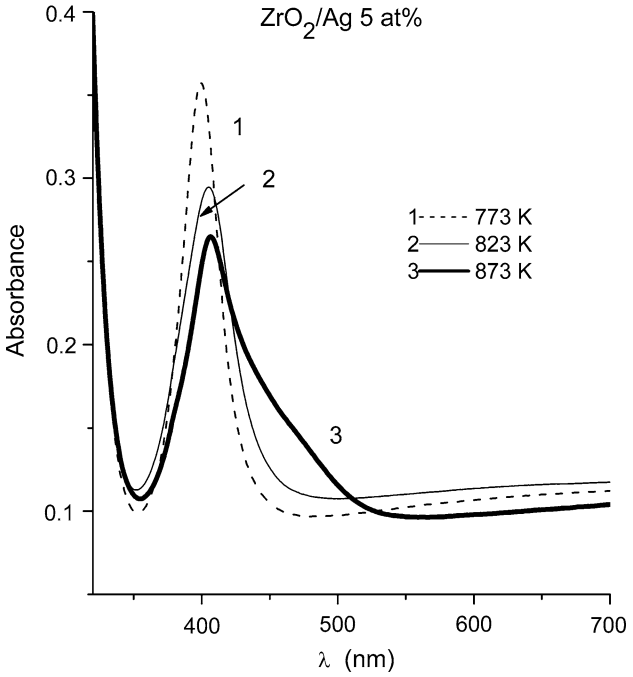

Fig. 11 Spectral changes in ZrO_2/Ag film depending on treatment temperature

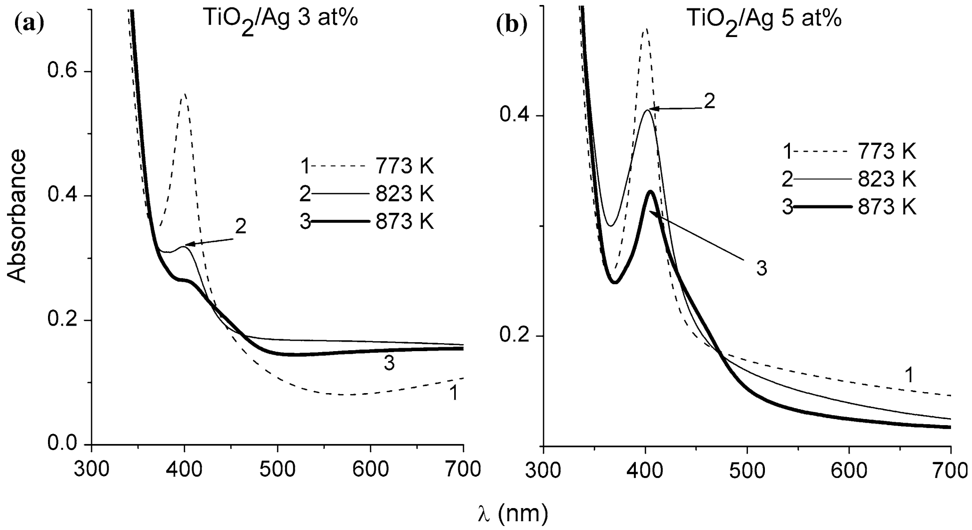

Fig. 12 Spectral changes in TiO$_2$/Ag films depending on treatment temperature

Elevating temperature (from 773 to 873 K) more weakly influences the absorbance of the titania/10 at.% Ag film than at lower silver content, probably due to a more uniform distribution of silver nanoparticles along the film profile. It causes diminishing of the influence of silver particles evaporation from the surface on general SPR band intensity (Figs. 12, 13). At 10 at.% Ag, silver nanoparticles exhibit almost similar optical behavior for all matrices (Fig. 13). The general tendency of the initial formation of silver nanoparticles in the outer layer of the film is

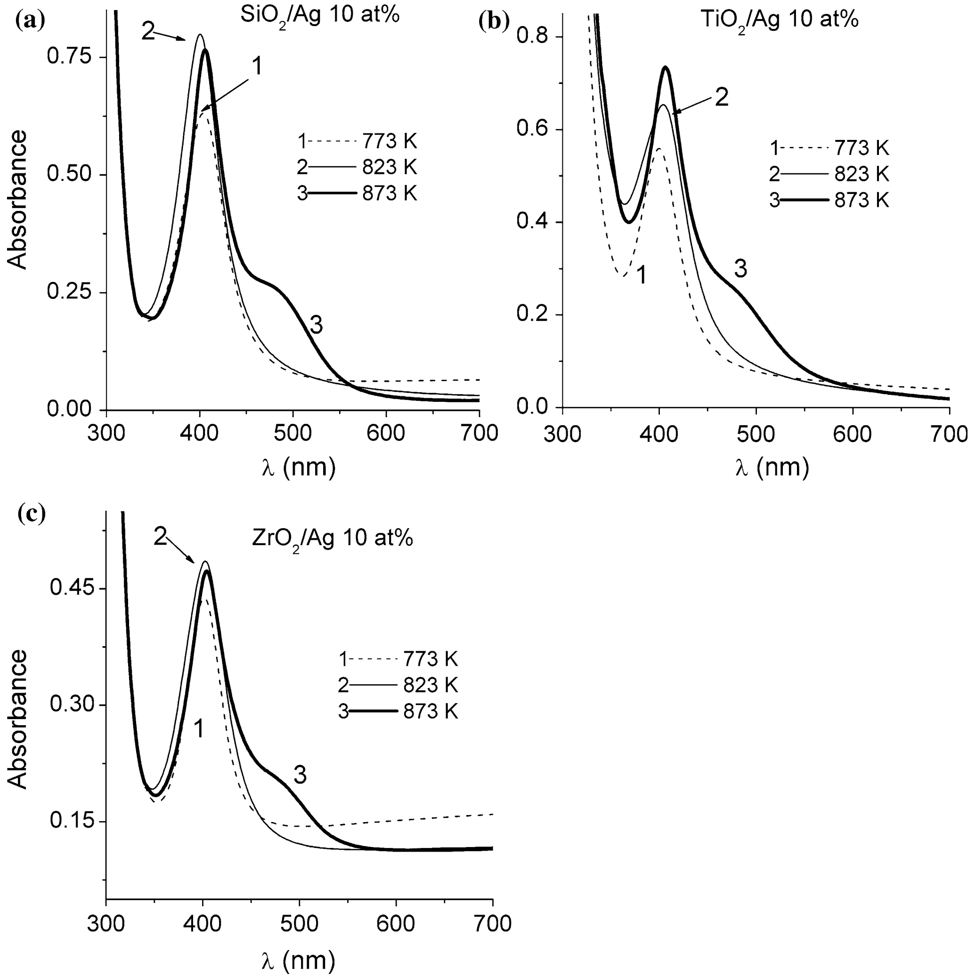

Fig. 13 Spectral changes in oxide films with initial loading of 10 at.% Ag depending on treatment temperature for matrices **a** SiO$_2$, **b** TiO$_2$, and **c** ZrO$_2$

specified by several factors. The first is the effects of hydrophilic–hydrophobic interaction. The second is the initiation of reduction of metal ions and charged cluster by volatile organics formed during template and ligand burning out and transfer of the reduced silver atoms and small clusters by the gaseous flow onto the outer surface. The third is steric factors in confined space of pores (which hinder nanoparticle growth), which are much weaker at the outer surface where the forces of mutual ions/atoms/nanoparticles interactions are smaller than within pores; i.e., particles have more freedom for their diffusion, clusterization, and agglomeration. With elevating temperature (873 K) organics are practically absent in the film, and further Ag^+ reduction proceeds due to electron attachment from the solid matrix with relatively narrow band gap (titania, zirconia). The process takes place both on the surface and in the volume of the film; however, at such high temperature, evaporation of Ag occurs effectively from the surface and is more difficult for Ag droplets formed within pores in the film volume.

4 Conclusion

Mesoporous silica, titania, and zirconia films were synthesized by the template sol–gel method at glass, silicon, and aluminum substrates. Pore structure in treated films undergoes smaller damages for silica because of its amorphous structure. In the case of titania and zirconia films, formation of oxide nanocrystallites leads to injury of the ordered mesostructure and the pore walls. However, the specific surface area and the porosity remain large after calcination of the films. Introduction of Ag^+ ions into the oxide film precursor results in enhanced injury of the mesostructure because of the formation of silver nanoparticles within pores on thermal treatment. However, in the case of the titania and zirconia films, silver can retard the crystallization of the matrices. Silver nanoparticles form dominantly on the outer surface of the film under lower sintering temperature if the amount of loaded silver is low. Matrix crystallization promotes silver embedding into the outer layer of the film. At a higher silver content (10%) and higher calcination temperature (873 K), silver nanoparticles could be distributed more uniformly along the film profile because of effective compensation of silver droplets evaporation from the outer film surface by nucleation and migrating processes of silver clusters within the film volume. Thus, nanocomposites with Ag nanoparticles/mesoporous oxide films could be synthesized with desirable morphological, textural, and structural characteristics of both components controlled due to variations in reaction media composition and treatment conditions.

Acknowledgment VMG is grateful to the STCU (grant no. 4481) for financial support.

References

1. Epifani M, Giannini C, Tapfer L, Vasanelli L (2000) J Am Ceram Soc 83:2385
2. He J, Ichinoze I, Kunitake T, Nakao A (2002) Langmuir 18:10005. doi:10.1021/la0260584
3. He C, Yu Y, Hu X, Larbot A (2002) Appl Surf Sci 200:239. doi:10.1016/S0169-4332(02)00927-3
4. Liz-Marzan LM, Giersig M, Mulvaney P (1996) Langmuir 12:4329. doi:10.1021/la9601871
5. Liu S, Zhang Z, Han M (2005) Anal Chem 77:2595. doi:10.1021/ac0482864
6. Chan Y, Zimmer JP, Stroh M, Steckel JS, Jain RK, Bawendi MG (2004) Adv Mater 16:2092. doi:10.1002/adma.200400237
7. Zhu Y, Shi J, Shen W, Dong X, Feng J, Ruan M, Li Y (2005) Angew Chem Int Ed 44:5083. doi:10.1002/anie.200501500
8. Song J-H, Atay T, Shi S, Urabe H, Nurmikko AV (2005) Nano Lett 5:1557. doi:10.1021/nl050813r
9. Fleischhaker F, Zentel R (2005) Chem Mater 17:1346. doi:10.1021/cm0481022
10. Behar-Levy H, Neumann O, Naaman R, Avnir D (2007) Adv Mater 19:1207. doi:10.1002/adma.200601702
11. Behar-Levy H, Avnir D (2005) Adv Funct Mater 15:1141. doi:10.1002/adfm.200400370
12. Blum J, Avnir D, Schuman H (1999) Chemtech 29:32
13. Shter GE, Behar-Levy H, Gelman V, Grader GS, Avnir D (2007) Adv Funct Mater 17:913. doi:10.1002/adfm.200600482
14. Yosef I, Avnir D (2006) Chem Mater 18:5890. doi:10.1021/cm0615368
15. Kelly LK, Coronado E, Zhao L, Schatz GC (2003) J Phys Chem B 107:668. doi:10.1021/jp026731y
16. Kreibig U, Vollmer M (1995) Optical properties of metal clusters. Springer, Berlin
17. Abu-Reziq R, Avnir D, Miloslavski I, Schumann H, Blum J (2002) J Mol Catal Chem 185:179. doi:10.1016/S1381-1169(02)00012-2
18. Shacham R, Mandler D, Avnir D (2004) Chem Eur J 10:1936. doi:10.1002/chem.200305469
19. Shacham R, Avnir D, Mandler D (2004) J Sol-Gel Sci Technol 31:329. doi:10.1023/B:JSST.0000048012.14882.38
20. Traversa E, Vona ML, Nunziante P, Licoccia S (2001) J Sol-Gel Sci Technol 22:115. doi:10.1023/A:1011276622863
21. Gonella F, Mattei G, Mazzoldi P, Battaglin G, Quaranta A, De G, Montecchi M (1999) Chem Mater 11:814. doi:10.1021/cm980749x
22. Krylova GV, Eremenko AM, Smirnova NP (2006) Fiz Khim Solid 7:50
23. Gnatyuk Y, Smirnova N, Eremenko A, Ilyin V (2005) Adsorpt Sci Technol 23:497. doi:10.1260/026361705774859893
24. Sanches C, Livage J, Henry M, Babonneau F (1988) J Non-Cryst Solids 100:65. doi:10.1016/0022-3093(88)90007-5
25. Gregg SJ, Sing KSW (1982) Adsorption, surface area and porosity, 2nd edn. Academic Press, London
26. Nguyen V, Do DD (1999) Langmuir 15:3608. doi:10.1021/la981140d
27. Gun'ko VM, Mikhalovsky SV (2004) Carbon 42:843. doi:10.1016/j.carbon.2004.01.059
28. Alberius P, Frindell K, Hayward R, Kramer E, Stucky G, Chmelka B (2002) Chem Mater 14:3284. doi:10.1021/cm011209u
29. Yang H, Kuperman A, Coombs N, Afara SM, Ozin GA (1996) Nature 379:703. doi:10.1038/379703a0

30. Yamada T, Asai K, Endo A, Zhou HS, Honma I (2000) J Mater Sci Lett 19:2167. doi:10.1023/A:1006704707758
31. Crepaldi EL, Soler-Illia GJ, Grosso D, Cagnol F, Ribot F, Sanchez C (2003) J Am Chem Soc 125:9770. doi:10.1021/ja030070g
32. Grosso D, Soler-Illia GJ, Babonneau F, Sanchez C, Albouy P-A, Brunet-Bruneau A, Balkenende AR (2001) Adv Mater 13:1085. doi:10.1002/1521-4095(200107)13:14<1085::AID-ADMA1085>3.0.CO;2-Q
33. Avnir D, Jaroniec M (1989) Langmuir 5:1431. doi:10.1021/la00090a032
34. Gun'ko VM, Turov VV, Turov AV, Zarko VI, Gerda VI, Yanishpolskii VV, Berezovska IS, Tertykh VA (2007) Cent Eur J Chem 5:420. doi:10.2478/s11532-007-0010-3
35. Cances MT, Mennucci B, Tomasi J (1997) J Chem Phys 107:3032. doi:10.1063/1.474659
36. Cossi M, Barone V, Mennucci B, Tomasi J (1998) Chem Phys Lett 286:253. doi:10.1016/S0009-2614(98)00106-7
37. Lukáč J, Klementová M, Bezdička P, Bakardjieva S, Šubrt J, Szatmáry L, Bastl Z, Jirkovský J (2007) Appl Catal B Environ 74:83. doi:10.1016/j.apcatb.2007.01.014
38. Zhang WF, He YL, Zhang MS, Yin Z, Chen Q (2000) J Phys D Appl Phys 33:912. doi:10.1088/0022-3727/33/8/305
39. Turković A, Ivanda M, Drašner A, Vraneša V, Peršin M (1991) Thin Solid Films 198:199. doi:10.1016/0040-6090(91)90338-X
40. Anandan C, Rajam KS (2008) Appl Surf Sci 254:2783. doi:10.1016/j.apsusc.2007.10.040
41. Di Paola A, Addamo M, Bellardita M, Cazzanelli E, Palmisano L (2007) Thin Solid Films 515:3527. doi:10.1016/j.tsf.2006.10.114
42. Goldstein GI, Newbury DE, Echlin P, Joy DC, Fiori C, Lifshin E (1981) Scanning electron microscopy and X-ray microanalysis. Plenum Press, New York
43. Henglein A (1998) Chem Mater 10:444. doi:10.1021/cm970613j
44. Link S, El-Sayed MA (2001) J Chem Phys 114:2362. doi:10.1063/1.1336140